Title

Dislocation Reduction and Stress Relaxation of GaN and InGaN Multiple Quantum Wells with Improved Performance via Serpentine Channel Patterned Mask

Journal

ACS Applied Materials & Interfaces, 8(33)

ISSN

1944-8244

Authors

Ji, Qingbin
Li, Lei
Zhang, Wei
et al.

Publication Date

2016-08-24

DOI

10.1021/acsami.6b07044

Peer reviewed

ACS APPLIED MATERIALS & INTERFACES

Research Article

www.acsami.org

Dislocation Reduction and Stress Relaxation of GaN and InGaN Multiple Quantum Wells with Improved Performance via Serpentine Channel Patterned Mask

Qingbin Ji,[†] Lei Li,[†] Wei Zhang,[‡] Jia Wang,[‡] Peichi Liu,[‡] Yahong Xie,[‡] Tongxing Yan,[†] Wei Yang,[†] Weihua Chen,*[,†] and Xiaodong Hu*[,†]

[†]State Key Laboratory for Artificial Microstructure and Microscopic Physics, School of Physics, Peking University, Beijing 100871, China

[‡]Department of Materials Science and Engineering, University of California ,Los Angeles, California 90095, United States

Supporting Information

ABSTRACT: The existence of high threading dislocation density (TDD) in GaN-based epilayers is a long unsolved problem, which hinders further applications of defect-sensitive GaN-based devices. Multiple-modulation of epitaxial lateral overgrowth (ELOG) is used to achieve high-quality GaN template on a novel serpentine channel patterned sapphire substrate (SCPSS). The dislocation blocking brought by the serpentine channel patterned mask, coupled with repeated dislocation bending, can reduce the dislocation density to a yet-to-be-optimized level of ~2×10^5 to 2×10^6 cm^{-2}. About 80% area utilization rate of GaN with low TDD and stress relaxation is obtained. The periodical variations of dislocation density, optical properties and residual stress in GaN-based epilayers on SCPSS are analyzed. The quantum efficiency of InGaN/GaN multiple quantum wells (MQWs) on it can be increased by 52% compared with the conventional sapphire substrate. The reduced nonradiative recombination centers, the enhanced carrier localization, and the suppressed quantum confined Stark effect, are the main determinants of improved luminous performance in MQWs on SCPSS. This developed ELOG on serpentine shaped mask needs no interruption and regrowth, which can be a promising candidate for the heteroepitaxy of semipolar/nonpolar GaN and GaAs with high quality.

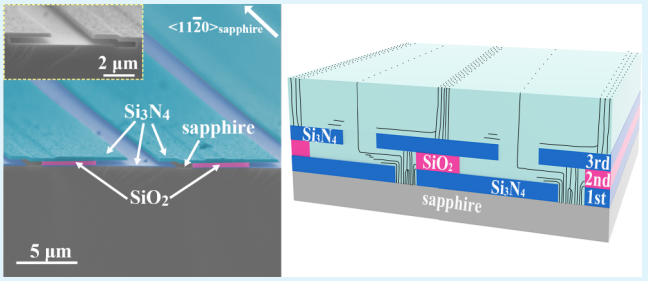

KEYWORDS: *GaN, epitaxial lateral overgrowth, serpentine channel mask, dislocation reduction, MOCVD, InGaN quantum well*

INTRODUCTION

III-Nitride compound semiconductors have attracted much interest and achieved tremendous progress in recent years. Considering the native substrate with large size is still not commercially available at low cost, GaN-based structures are usually grown on sapphire, Si and SiC substrates by heteroepitaxy. However, high-density structural defects are generated in GaN epilayers because of the large lattice and thermal mismatches between GaN and these heterosubstrates.[1] These defects can act as nonradiative recombination sites, carrier scattering centers, current leakage paths, etc.[2−6] The electrical and optical qualities, such as device lifetime, electron mobility, current leakage, and quantum efficiency of GaN-based devices are deteriorated, which are very important to laser diode, high electron mobility transistor, photodetector, and UV light-emitting diode (LED).[2−6] Obviously, it is urgent and challenging to effectively diminish the defect density in GaN template for the subsequent growth of InGaN and AlGaN alloys.

Many growth techniques have been utilized to reduce extended defect densities in GaN. One of the most common and promising methods is epitaxial lateral overgrowth (ELOG) and its derivatives, such as pendeo-epitaxy (PE) and facet-controlled epitaxial lateral overgrowth (FACELO).[1,7,8] In situ/ex situ micro/nanoscale SiN_x/SiO_2 patterned masks or patterned substrates with stripe, column, sphere, cone shapes and etc are usually uesd.[1,2,7−11] Latest attempts using the hybrid substrates coated with carbon nanotubes, graphene, and boron nitride have been proposed.[12−14] The laterally grown areas (wing region) are nearly defect-free, since the propagation of structural defects beneath the mask can be directly blocked. However, defects which come from the coherently grown GaN, still propagate above the openings of the mask, leading to highly faulted window region by most of ELOG methods. Further defect reduction in window region is obtained by introducing the defect bending, which is tailored to form triangular pyramidal facets via growth conditions.[1,7] It is proved to be efficient for threading dislocations in polar GaN. As for nonpolar/semipolar GaN, the defects such as basal plane stacking faults (BSFs), prismatic plane-stacking faults (PSFs),

Received: June 11, 2016
Accepted: August 3, 2016

DOI: 10.1021/acsami.6b07044
ACS Appl. Mater. Interfaces XXXX, XXX, XXX−XXX

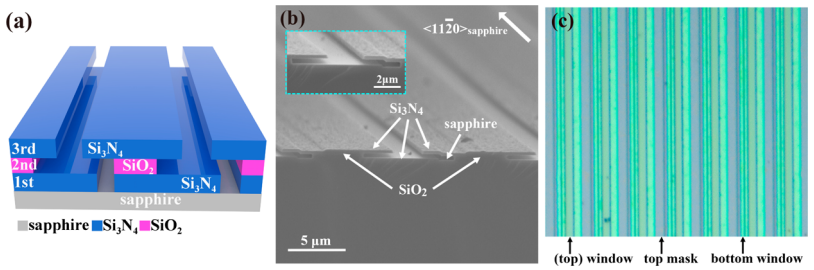

Figure 1. (a) Schematic illustration of SCPSS. (b) SEM image (45° tilted) of SCPSS. A close-up view of the serpentine channel mask is shown in inset. The window stripes oriented along <11$\bar{2}$0>$_{sapphire}$ direction with a total channel height of ~700−800 nm are observed. (c) Plan-view OM image of SCPSS. The widths for the open windows of the first (bottom) and third (top) Si_3N_4 layers are ~2−4 μm and ~1−2 μm, respectively.

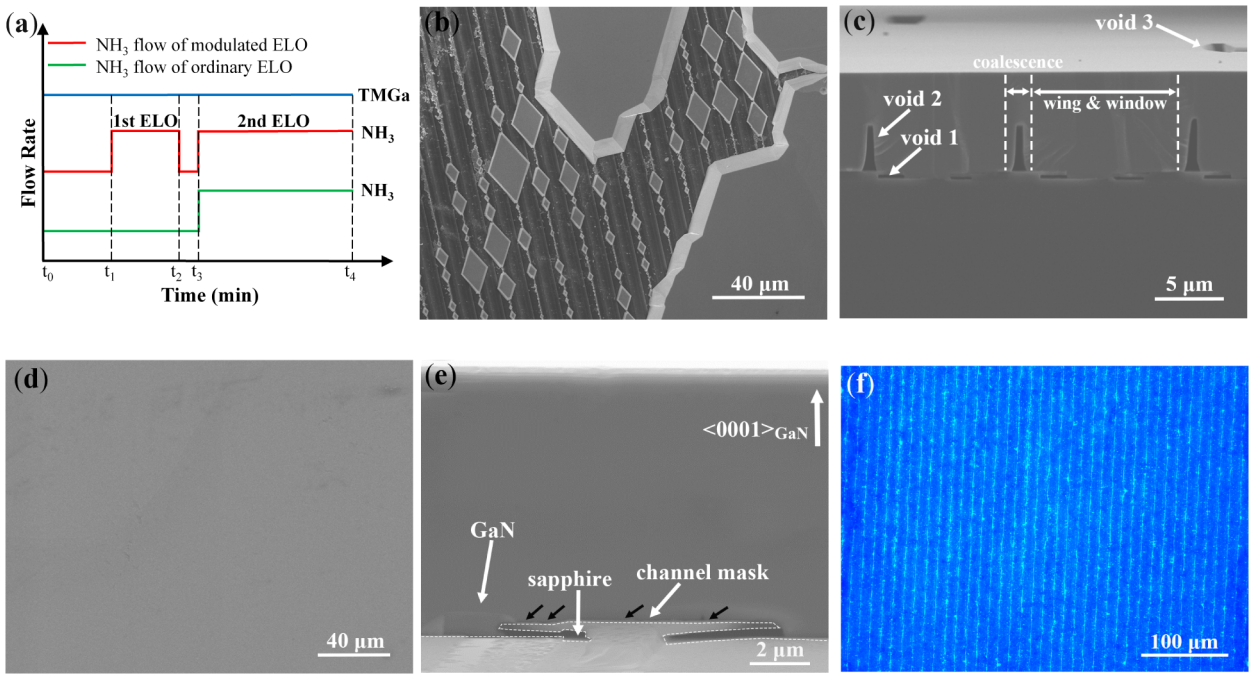

Figure 2. (a) Flow patterns of TMGa and NH_3 for the ordinary and modulated ELO methods of GaN growth on SCPSS. (b, c) Plan-view and cross-sectional SEM images of as-grown noncoalesced GaN film on SCPSS by the ordinary ELO method. Window, wing, coalescence regions are separated by dashed lines. The large voids are indicated by one-way white arrows. (d, e) Plan-view and cross-sectional SEM images of as-grown completely coalesced GaN film on SCPSS by the modulated ELO method. Only narrow and tiny voids (marked by black arrows) are seen over the mask (labeled with dashed lines) (f) Plan-view fluorescent micrograph of GaN surface on SCPSS by the modulated ELO method.

partial dislocations (PDs), are situated on specific planes.[15,16] In this case, the bending of stacking faults is not possible, and the defect filtering should be therefore limited using these techniques.

Hence, we propose an innovative serpentine channel patterned mask, and aim to make the most use of mechanical blocking effect by mask geometry, which is independent of the nature of the defects. In the meantime, bending effect of defects can also be enhanced. In particular, even if the dislocation bending is ineffective in the cases just mentioned, the blocking mechanism can still make the main contribution to the defect annihilation in window region.

In this work, we apply the serpentine channel patterned mask to *c*-plane sapphire substrate (SCPSS, Figure 1a). ELOG of GaN template with no need for regrowth, and InGaN/GaN multiple quantum wells (MQWs) have been achieved. GaN template on SCPSS contains a low dislocation density of ~2×10^5 to 2×10^6 cm^{-2}, comparable to that by freestanding GaN homoepitaxy.[17−19] Local optical properties as well as stress distributions of GaN epilayers in different regions have been examined. The correlations between the modulated ELO process and the observed dislocation annihilation and stress relaxation are also established. Especially, a dramatic decrease in the defect density is demonstrated in both wing and window regions on SCPSS, expanding the contiguous area with low dislocation density, compared to most other ELOG techniques with two highly defective regions. The performance of MQWs grown on SCPSS is greatly improved in comparison with the reference sample on conventional sapphire substrate (CSS).

EXPERIMENTAL SECTION

The Si_3N_4 and SiO_2 three-layer stack of the serpentine channel patterned mask is clearly confirmed by the scanning electron microscopy (SEM) image and optical microscopy (OM) image in Figure 1b, c. Details of mask fabrication can be found in the Supporting Information. The ELO of GaN on SCPSS was conducted in a Thomas Swan close-coupled showerhead metal−organic chemical vapor deposition (MOCVD) system. Trimethylgallium (TMGa) and ammonia (NH_3) were used as precursors of Ga and N with hydrogen (H_2) as the carrier gas. The temperature was at first set to 530 °C for 3−10 min to grow the GaN nucleation layer. The growth temperature,

DOI: 10.1021/acsami.6b07044
ACS Appl. Mater. Interfaces XXXX, XXX, XXX−XXX

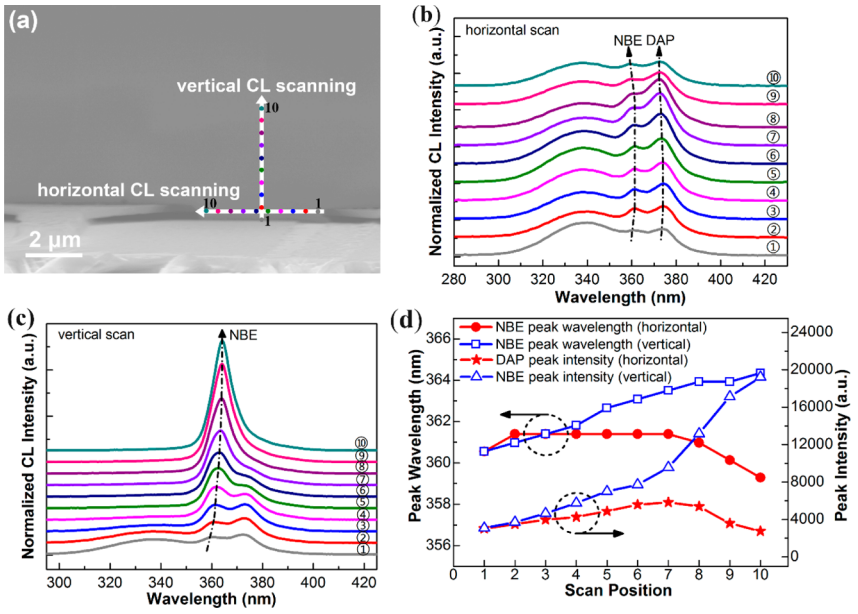

Figure 3. (a) Cross-sectional SEM image of fully coalesced GaN on SCPSS. Arrows show the directions of CL linescans performed parallel and perpendicular to the substrate surface. CL spectra of different positions (position 1−10) collected along the (b) horizontal and (c) vertical directions, respectively. (d) Variations in wavelength and intensity of CL peaks for GaN, revealing the crystal and strain changes during the ELO process.

and pressure for ELO process were varied from 1040 to 1060 °C, and from 75 to 200 Torr. Because of the excellent nucleation selectivity of GaN over crystalline sapphire surface, the GaN growth started from the exposed sapphire windows of first layer rather than the amorphous surface of SiO_2 or Si_3N_4. As GaN grew from the first mask to the third mask layer, modulated ELO method was adopted to obtain the fully coalescent GaN template. For comparison, 7.5 μm thick GaN films were grown on SCPSS and CSS, followed by the identical LED structures, consisting of 2 μm undoped GaN, 3 μm n-type GaN, 10-period InGaN/GaN MQWs, and 200 nm p-type GaN.

Surface morphologies and microstructural properties of the samples were characterized by SEM and cathodoluminescence (CL) spectroscopy in an FEI Quanta 200F equipped with a Gatan MonoCL3 system. Micro-Raman measurements were carried out using a HORIBA JY-T64000 Raman microscope with the 514.5 nm excitation line from an Ar laser. Transmission electron microscopy (TEM) was performed in an FEI Titan 80−300. All above studies were operated at room temperature (RT). The optical performance was analyzed by photoluminescence (PL) spectroscopy, including temperature-dependent PL and time-resolved PL measurements in an evacuated chamber of a closed-cycle helium cryostat in the temperature range of 10−300 K, and power-dependent PL measurements at RT.

RESULTS AND DISCUSSION

The optimized ELO condition is critical to the full and fast coalescence of GaN islands. Figure 2a depicts the ordinary and modulated ELO methods for GaN growth on SCPSS. The difference lies in the V/III ratio, i.e., by varying NH_3 flow rate, while keeping TMGa flow rate identical. High and low V/III ratios can adjust growth anisotropy, and enhance the lateral and vertical growth rates, respectively.[20] In the modulated ELO method (red line), the lateral growth rate was constantly modulated by changing the V/III ratio according to the shape of serpentine channel. The processes with high V/III ratio between t_1 and t_2, t_3 and t_4, are associated with GaN growth over the first bottom Si_3N_4 (first ELO) and the third top Si_3N_4 (second ELO), respectively. By ordinary ELO method, after the fixed and low V/III ratio for growth inside the channel (t_0−t_3) and final ELO step (t_3−t_4), GaN film is partially coalescent, as presented in the plan-view SEM image of Figure 2b. From the area not entirely covered by GaN, we can observe GaN islands emerging from the bottom windows of the channel mask. It suggests GaN does selectively nucleate on the bare sapphire of bottom window instead of the amorphous Si_3N_4 mask and the reaction precursors can reach the deposition surface through the channel. GaN growth is blocked by the top Si_3N_4 layer because of insufficient lateral growth within the region of the second SiO_2 layer. Figure 2c displays the cross-sectional SEM image of the partially coalescent GaN film with a total thickness of ~7 μm. The voids within the mask (void 1) indicate the lateral growth rate is not fast enough to fill the channels. After growth of ~3.6 μm GaN, the coalescence of GaN arises and the voids over the top Si_3N_4 layer (void 2) disappear. But there still remains some voids on the surface of GaN film (void 3), which reveals the difficulty of coalescence using the nonoptimized ELO growth.

By means of the modulated ELO method, the film surface is mirror-like smooth in the plan-view SEM image of Figure 2d, confirming that the fully coalescent and flat GaN is obtained over whole SCPSS. As shown in the cross-sectional SEM image of Figure 2e, GaN ELO layer has a total thickness similar to that in Figure 2c. The channel mask is labeled with white dashed lines. No large voids are seen in coalescent fronts, except tiny voids (marked by black arrows) at interface of the third Si_3N_4 layer, suggesting an easy and fast coalescence. Figure 2f shows the fluorescent microscopy image of the as-grown GaN surface. In contrast to the dark blue colored wing and window regions, light blue colored sharp and parallel lines are located in coalescent fronts, which are caused by the defect-related yellow band emission.[21]

To further understand the modulated ELO process, microstructural properties of selectively grown GaN were analyzed by cross-sectional CL linescan at RT under 15 kV. Figure 3a shows the spatial CL profiles recorded perpendicular and parallel to the substrate surface. The emission centered at ~361 nm (3.44 eV) is ascribed to near band edge (NBE) emission of GaN. The other emission centered at ~372 nm (3.33 eV) can be assigned to the donor−acceptor-pair (DAP)

DOI: 10.1021/acsami.6b07044
ACS Appl. Mater. Interfaces XXXX, XXX, XXX−XXX

transitions arising from impurities or point defects during ELO process.[22] The blue-shifted extremely broad (e−h) plasma emission around 340 nm (3.65 eV) is observed, indicating a high local free carrier concentration of GaN in the channel due to the strong unintentional doping.[23,24] When the electron beam moves from the right to the left side of GaN in the channel, as illustrated in Figure 3b, d, the intensity of DAP peak initially increases and then decreases, which agrees with the modulated ELO process by tuning the V/III ratio in Figure 2a. After GaN grew out of the bottom window, V/III ratio was driven to a much higher value for further lateral growth over the first Si_3N_4 layer, which could contribute to the acceptor-like Ga vacancies (V_{Ga}).[22] The defects caused by the high V/III ratio, accumulated until the V/III ratio was lowered for the subsequent vertical growth inside the top window. The position having the maximum DAP intensity not only is associated with GaN featuring the highest defect accumulation in the channel, but also corresponds to the high-to-low shift in V/III ratio prepared for the following vertical growth. Moreover, the wavelength of NBE peak gets shorter in the vicinity of the right and left edges of the top mask opening, while that in the middle of the top opening is longer and remains unchanged. The fact that NBE emission is shifted to higher energy can be explained by the Burstein−Moss effect, caused by the increased concentration of free carriers near the Si_3N_4 and SiO_2 mask.[17,21,25] The CL line scanning from channel upward to surface, was employed to study the optical properties and residual strain. As clearly shown in Figure 3c, d, the fwhm of NBE peak becomes narrower and the intensity keeps increasing as GaN grows along the *c*-axis direction, while the (e−h) plasma and DAP peaks gradually disappear. Such obvious changes in CL spectra prove the improved crystal quality of GaN grown over the whole mask, with drastically reduced impurities and free carriers. The NBE peak also displays a remarkable red shift of 3.79 nm (35.8 meV) along the vertical direction. It reveals that the compressive stress of GaN is relaxed by 0.86 GPa with growth going on by adopting the band gap pressure coefficient (41.4 meV/GPa).[26] In conclusion, the improved crystal quality and relaxed stress of GaN are observed after growth emerging from the channel.

Defect- selective etchings were carried out in molten KOH for 6 min at 280 °C to reveal the density of dislocations threading to the surface of GaN templates. Figure 4a, b shows the typical plan-view SEM images of the etched GaN epilayers grown on SCPSS and CSS, respectively. Most of the etch pits are aligned within coalescence regions, organizing along lines parallel to the stripe orientation $\langle 11\bar{2}0\rangle_{sapphire}$, whereas window and wing regions are nearly free of etch pits. The etch-pit density (EPD) of coalescence region is measured ~2−3 × 10^6 cm^{-2}. And this density decreases down to ~2−3 × 10^5 cm^{-2} in the area between coalescence boundaries, which is 2 orders of magnitude less than the EPD (~1 × 10^7 cm^{-2}) in GaN template on CSS shown in Figure 4b. Every etch pit corresponds to a TD, reflecting the spatial distribution of TDs in GaN.[27] It clearly confirms that the TDs can be effectively reduced by the serpentine channel patterned mask. GaN template grown on SCPSS has an average TDD of ~3−5 × 10^5 cm^{-2}, which is close to the level of freestanding GaN homoepitaxy, PE, and FACELO,[7,8,17] and approximately 1 order of magnitude less than most of the other ELOG methods.[1,9] The EPD estimated here using molten KOH is consistent with the etch-pit result after mixture solution of H_2SO_4 and H_3PO_4 etching at 160 °C in our previous work

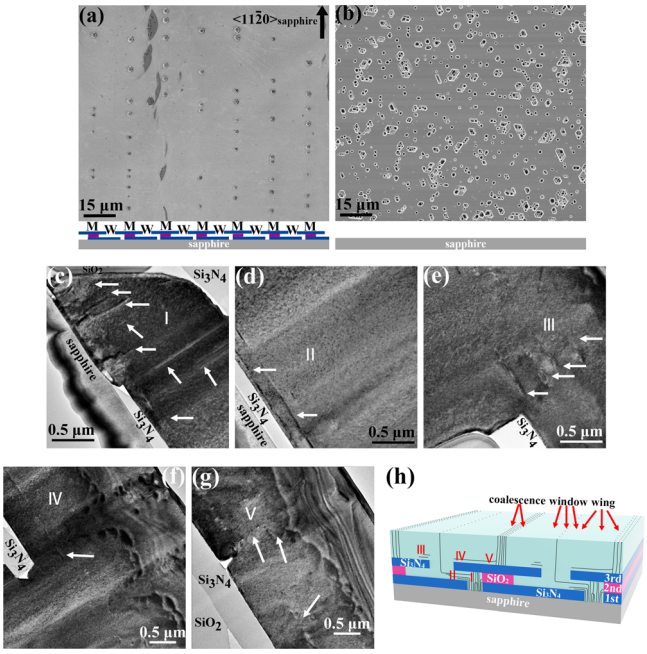

Figure 4. Plan-view SEM images of the etched GaN surface on (a) SCPSS and on (b) CSS after molten KOH etching at 280 °C for 6 min. The top Si_3N_4 mask layer and top window of SCPSS are labeled by symbol M and W, respectively. (c−g) Cross-sectional TEM bright-field images with $[01\bar{1}0]$ zone axis and [0000] diffraction vector of region *I*−*V* on SCPSS, corresponding to regions indicated by red numerals in h. Dislocations are denoted by white arrows. (h) Schematic diagram of dislocation evolution for GaN grown on SCPSS. Continuous black lines represent dislocations.

(~4−7 × 10^5 cm^{-2}).[28,29] Hence, within a certain tolerance, wing and window regions can be used as a whole for high-quality device fabrication, which accounts for about 80% of the total area.

To explain the dislocation annihilation processes in GaN on SCPSS, cross-sectional TEM measurement along $[01\bar{1}0]$ zone axis was employed. The TEM bright-field images of GaN inside and outside the channel are presented in Figure 4c−g, corresponding to region *I*−*V* marked by red numerals in Figure 4h. As seen in Figure 4c (region I), a large number of dislocations (white arrows) are generated at the GaN/sapphire interface in the bottom windows due to lattice mismatch. However, most of them terminate inside the serpentine channel mask, some of which interact with each other and form annihilation loops, whereas others propagating vertically are blocked by the overhanging top Si_3N_4 mask. Moreover, because of the image force of mask,[30] dislocations can potentially bend 90°, then propagate laterally in parallel to the Si_3N_4 mask layer, and finally terminate at both ends of channel (see Figure 4c, d). No TDs perpendicular to mask surface are seen in region III and IV. It indicates TDDs in wing and window regions are below the images' resolutions of ~5 × 10^6 cm^{-2}.[16] Only few dislocations running laterally are observed atop the edges of Si_3N_4 mask (Figure 4e, f). This might be explained by the basal plane stacking faults associated with the surface structure imperfection.[31] These horizontal dislocations terminate in region V and combine with other TDs at the coalescence boundary owing to the inevitable tilt of crystal planes (Figure 4g).[32] The dislocation evolution is summarized in Figure 4h. Only very few dislocations can emerge from the top window and thread to GaN surface after blocking and bending inside

DOI: 10.1021/acsami.6b07044
ACS Appl. Mater. Interfaces XXXX, XXX, XXX−XXX

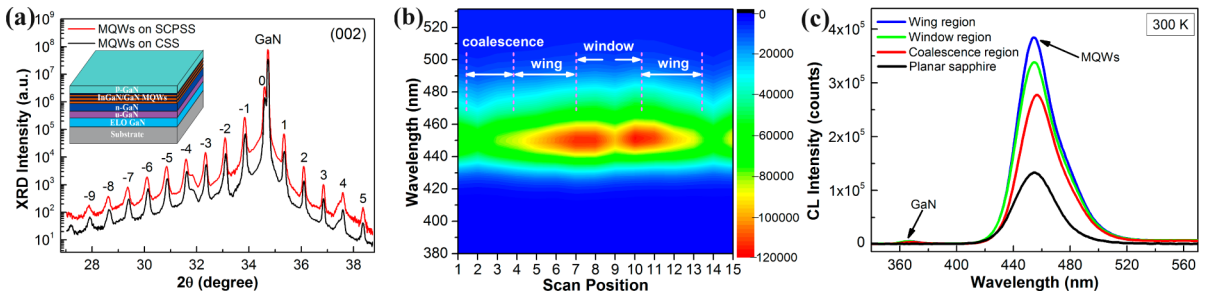

Figure 5. (a) HRXRD $\omega-2\theta$ scans of the (0002) reflection for MQWs grown on SCPSS-based and CSS-based GaN template. Inset: schematic illustration of the LED structure. (b) Intensity map of MQW emission measured by CL linescan under 15 kV at RT within a mask period on SCPSS, as denoted by dashed pink lines. (c) CL spectra recorded from three typical regions on SCPSS and region on CSS with the same area $2 \times 2\ \mu m^2$.

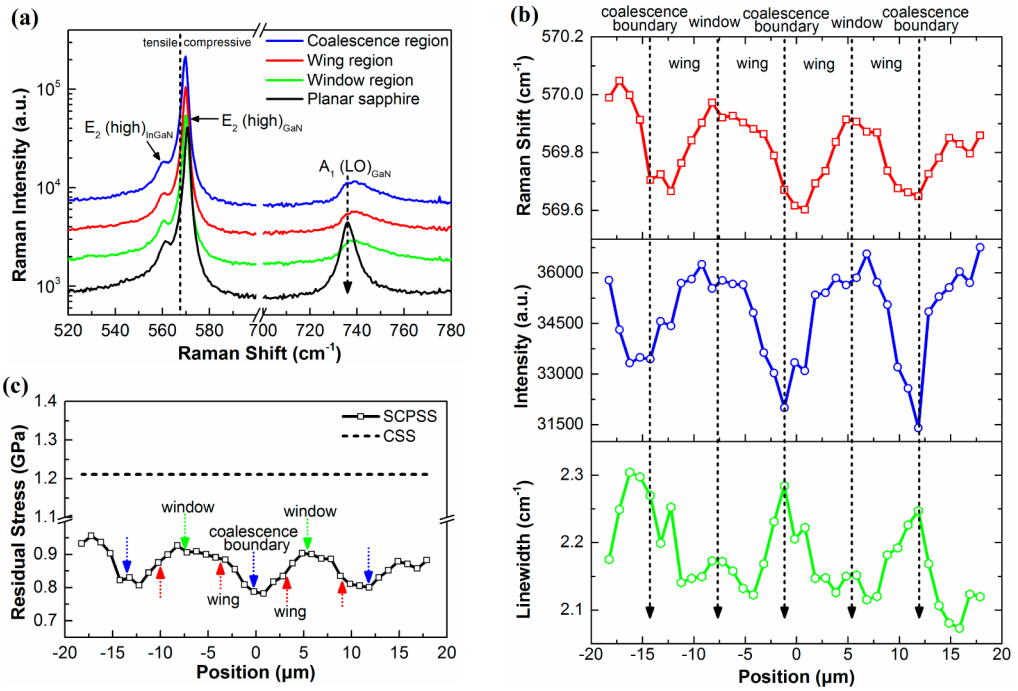

Figure 6. (a) Representative Raman spectra obtained from window, wing, coalescence regions on SCPSS and region on CSS. Black dashed line denotes the E_2 (high) phonon frequency of strain-free GaN (b) Raman line-scan profile of the GaN E_2 (high) phonon mode across the mask tripe orientation, including phonon frequency, intensity, and line width variations as a function of position. (c) Stress distribution of the SCPSS-based MQW sample is compared with the CSS-based MQW sample.

the channel. That explains why window region features low TDD and reduced defect area. Eventually, TDs are the most prominent at the coalescence fronts. Types of dislocations in different regions can be identified from the cross-sectional TEM images with different two-beam conditions (Figures S2 and S3). Therefore, the blocking and bending of dislocations brought by the serpentine channel act synergistically for the effective dislocation filtering in wing and window regions.

Figure 5a presents the high-resolution X-ray diffraction (HRXRD) $\omega-2\theta$ scans for the (0002) plane of LED structures on the as-grown GaN templates (schematic shown in inset), which were measured at Beijing Synchrotron Radiation Facility (BSRF). Well-resolved narrow satellite peaks up to ninth order can be clearly distinguished, confirming the excellent periodicity and sharp interfaces of the MQWs on SCPSS and CSS. The indium content for the InGaN QW is calculated to be 21.7% on SCPSS, which is greater than 19.6% on CSS. As reported by many groups, the strain in GaN template has an obvious influence on the indium incorporation of the subsequent InGaN growth.[33−36] Here, the increased indium composition of InGaN QW is attributed to the higher indium incorporation due to the strain relaxation in GaN template on SCPSS, which will be proved by the following Raman analysis. To gain insight into the microscopic optical properties, we took on spatially and spectrally resolved CL studies under accelerating voltage of 12.5 kV at RT. CL line scan was utilized to measure the SCPSS-based MQW sample within a full mask period. The line scan data in Figure 5b is displayed by an intensity map of MQW emission in different positions. The area ratios determined by the intensity difference in one mask period, are 28, 52, and 20% for window, wing, and coalescence regions, respectively. In terms of window region, only the small center part exhibits a slightly lower intensity than the rest two sides by 12%. Moreover, for wing region, the CL intensity decreases gradually as approaching the wing-coalescence interface. The average intensity in wing region is similar to that in window region, whereas the intensity in coalescence region is considerably weaker. This characteristic contrast in

DOI: 10.1021/acsami.6b07044
ACS Appl. Mater. Interfaces XXXX, XXX, XXX−XXX

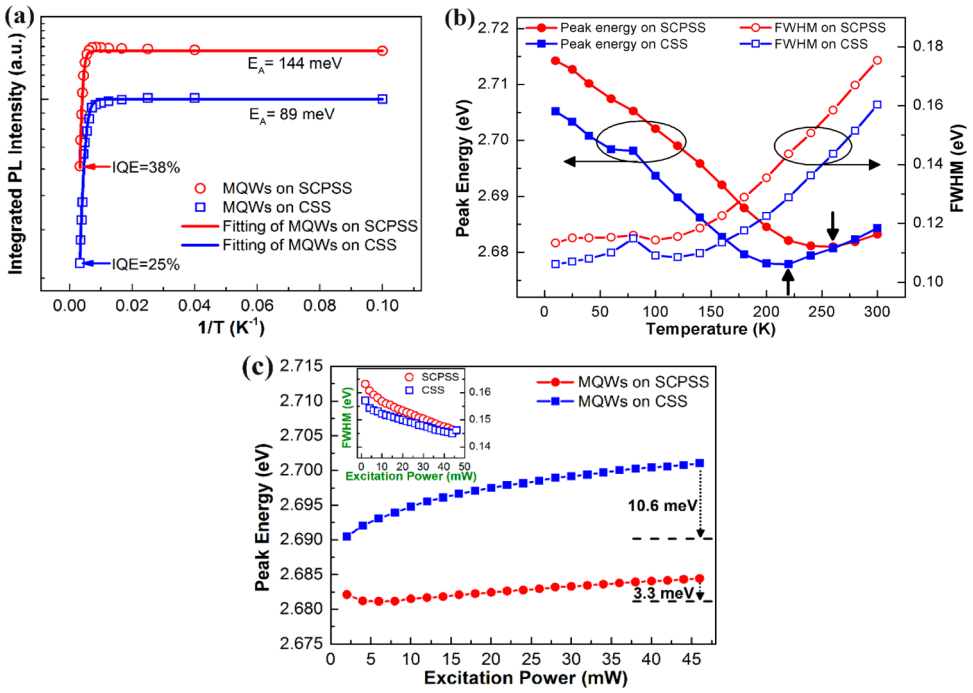

Figure 7. (a) Normalized integrated PL intensity of MQW emission as a function of temperature from 10 to 300 K for the MQW samples on SCPSS and CSS, with the best fitting of the Arrhenius plots based on eq 1. (b) Peak energy and fwhm of PL as a function of temperature for the two samples. (c) Variations in peak energy and fwhm (in inset) with excitation power ranging from 2 to 46 mW measured at RT.

intensity demonstrates that the optical properties are quite sensitive to the spatial variations of crystal quality, which is well consistent with the dislocation distribution on SCPSS. Figure 5c shows the CL spectra of different regions with the same area of 2 × 2 μm^2, which were all excited and collected under the same conditions. The dominant peaks near 455 nm (2.727 eV) are emitted from InGaN/GaN MQWs. The integrated CL intensities in wing, window, and coalescence regions on SCPSS are 2.9, 2.6, and 2.1 times those on CSS, respectively. All three regions on SCPSS show enhanced MQW emissions than the region on CSS, among which wing region is the most pronounced. It is evident that the luminescence intensity of the MQW structure is greatly improved on SCPSS. In addition to the low dislocation density,[3] the stress state is believed to be another key factor influencing the quantum efficiency of InGaN/GaN LEDs.[13,14]

To further verify the spatial variations in stress state and crystalline quality, micro-Raman measurements were performed with ∼1 μm spatial resolution in the z(xu)z configuration. Figure 6a shows the representative Raman spectra extracted from regions of the SCPSS-based and CSS-based MQW samples. The prominent peaks associated with the E_2 (high) and A_1 (LO) phonon modes of GaN are symmetry-allowed.[25] Frequencies of the E_2 (high) mode are 570.0, 569.9, 569.6, and 570.7 cm^{-1} for GaN on window, wing, coalescence regions of SCPSS and on CSS, respectively. Compared with the standard E_2 (high) frequency 567.6 cm^{-1} of the unstrained GaN,[13] the E_2 (high) frequency of GaN on CSS shows the maximum blue-shift (3.1 cm^{-1}), whereas the minimum blue-shift (2.0 cm^{-1}) occurs in coalescence region on SCPSS. It reveals that regions on SCPSS and CSS have different statuses of the compressive strain, which will be discussed in Figure 6b. The A_1 (LO) mode of GaN on CSS has a nearly symmetric peak centered at 736.2 cm^{-1}. On the other hand, the A_1 (LO) modes on SCPSS are shifted upward with asymmetric and broadened peak shapes. It can be attributed to (i) mixing of the A_1 (LO) with the E_1 (LO) phonon mode due to the crystallographic tilt of ELO layer[32] (ii) LO phonon-plasmon coupling enhanced by the diffusion of Si atoms from the Si_3N_4 and SiO_2 masks besides n-doped GaN.[25,37] The shoulder peaks of phonon modes at ∼561 cm^{-1} are observed on both SCPSS and CSS. They should mainly come from the E_2 (high) modes of InGaN layers in MQWs.[38] The contributions of the symmetry-forbidden E_1 (TO) modes at ∼559 cm^{-1} are relatively small here. Otherwise, the peak at ∼561 cm^{-1} should have noticeable changes on CSS under a perfect backscattering geometry. Micro-Raman line-scan was performed along the direction perpendicular to the mask stripe orientation of SCPSS. In Figure 6b, the line profile of E_2 (high) phonon mode shows periodic variations throughout the surface. The biaxial stress can be calculated by $\Delta\omega = K\sigma_{xx}$, where $\Delta\omega$ is the measured Raman frequency shift of E_2 (high) mode with respect to the unstrained GaN and the stress coefficient K of 2.56 cm^{-1}/GPa.[13] As shown in Figure 6c, GaN on CSS suffers the most compressive stress (1.21 GPa) as a result of the lattice and thermal mismatch. By contrast, GaN on SCPSS experiences some levels of stress relaxations in different regions. The minimum relaxation locates in the center of window region with the stress reduced to 0.93 GPa. GaN in the top window actually arises from the vertical growth of the first ELO layer inside the channel. There is no direct contact with the exposed sapphire which helps relieve some strain.[37] A minor deterioration of the crystal quality is observed only in the center of window region, which is discerned from the slightly decreased intensity and increased line width of the E_2 (high) phonon as compared to the edge area of window region. This indicates again the improved crystal quality in window region compared with the conventional ELOG. During the second ELO step, the E_2 (high) frequency gradually decreases by only 0.2 cm^{-1} from the center of window to wing region. Thus, further strain relaxation is continued in wing region and the

DOI: 10.1021/acsami.6b07044
ACS Appl. Mater. Interfaces XXXX, XXX, XXX−XXX

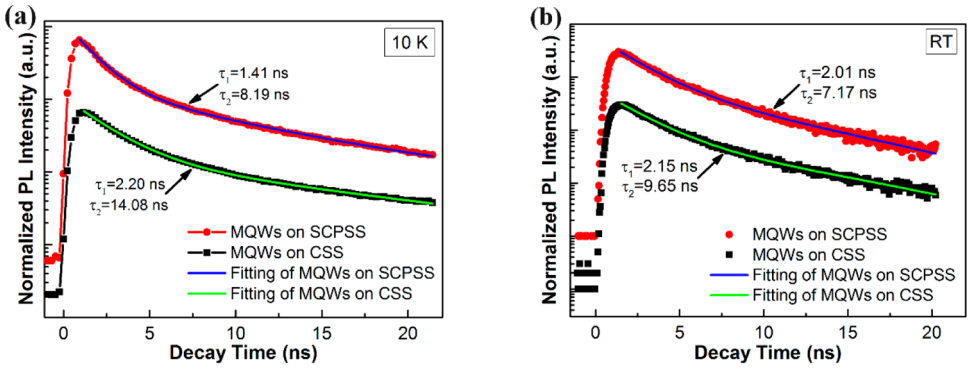

Figure 8. Experimental and fitted traces of time-resolved PL measurements for the MQW samples on SCPSS and on CSS taken under the respective PL peak energies at (a) 10 K and at (b) RT. The fast decay time and the slow decay time listed in the plots are fitted by biexponential decaying function eq 2.

stress value is lower (0.90−0.86 GPa). When approaching the coalescence region, the E_2 (high) phonon in wing region has slightly weaker intensity and larger line width than that at the window-wing boundary. It is mostly due to the accumulated crystallographic imperfection in GaN over the Si_3N_4 mask.[10] Particularly, the significant stress relaxation occurs at the coalescence boundary with the minimum stress of 0.78 GPa, which may result from the increased dislocations and Si-dopant at the meeting fronts.[10,33] The maximum line width and minimum intensity of the E_2 (high) phonon also prove that the dislocations and the wing tilt are most prominent in coalescence region. Thus, large contiguous area of GaN (wing and window regions) with low dislocation density and less residual stress is obtained on SCPSS.

To assess the enhancement of internal quantum efficiency (IQE), temperature-dependent PL (TDPL) measurements were carried out from 10 to 300 K by using a 405 nm laser as the excitation source. The normalized integrated PL intensities of MQW emission as a function of temperature, together with the fittings of the Arrhenius plots, are summarized in Figure 7a. The IQE can be estimated by the integrated PL intensity ratio of 300 to 10 K ($I_{300\ K}/I_{10K}$), assuming the quantum efficiency at 10 K is unity.[39] A great enhancement of 52% is gained, as the IQE of MQWs is calculated to be 38% on SCPSS and 25% on CSS. The discussion about the nonradiative recombination is performed by fitting the Arrhenius equation as follows

$$I(T) \propto \frac{1}{1 + \sum_i C_i \exp(-E_{Ai}/k_B T)} \quad (1)$$

where $I(T)$ is the normalized integrated PL intensity, E_{Ai} represents the activation energies of the nonradiative recombination centers. C_i is the rate constants, and K_B is Boltzmann's constant.[39,40] We note that the integrated PL intensity drops rapidly only in high-temperature range for both samples. So the single nonradiative recombination channel is used for best fittings. Here, the large activation energy E_A is referred to the localization energy barrier between the localized potential minima and the nonradiative recombination centers, taking charge of the dominant thermal quenching of the PL intensity in high-temperature range.[14,41] The E_A of MQWs on SCPSS and CSS are 144 and 89 meV, respectively. The larger value of E_A on SCPSS indicates a higher energy barrier for carriers captured by the nonradiative recombination centers, which is due to the greatly reduced TDs in ELO GaN.[34,40]

In low-temperature range, the integrated PL intensity on CSS drops slightly with temperature, whereas that on SCPSS shows almost no decrease. It should be related to the different carrier localization degrees.[14,34] To clarify this, the peak energy and fwhm of the MQW emission at different temperatures shown in Figure 7b are analyzed. At 10 K, a higher peak energy of MQWs on SCPSS is primarily contributed by the reduced piezoelectric field, though the average indium content calculated is slightly higher than that on CSS. The broader fwhm can be explained by the small differences of indium content among three regions on SCPSS since we did not use micro-PL system. For both samples, the peak energy is redshifted up to around 220 K, and then blueshifted with temperature up to 300 K. This S-shaped temperature dependence of peak energy is typical in InGaN-related emission and is the evidence of localization states.[42−44] At very low temperature, photoexcited carriers are randomly distributed among the localized states. As temperature rises (25−220 K), the weakly localized carriers are thermally activated and have more opportunity to relax down into the lower energy tail states via hopping, resulting in the initial redshift of peak energy. Then as temperature further increases to 300 K, the localized carriers have enough thermal energy (k_BT) to populate higher energy states, causing the blueshift and increased fwhm. Specifically, transition from redshift to blueshift of peak energy occurs at 260 K on SCPSS, which is higher than 220 K on CSS. It reveals that the localized carriers in MQWs on SCPSS need higher transition temperature, i.e., higher thermal energy to transfer to higher energy states, which is caused by a stronger carrier localization effect of MQWs on SCPSS.[44−46] Compared to MQWs on CSS, the higher transition temperature and the slower rate of blueshift with temperature on SCPSS, result in the crossover of peak energies at 270 K, and finally slightly lower peak energy at 300 K (RT). Previous study shows that the high crystal quality of GaN substrate leads to narrow and deep potential valleys accompanied by the enhanced localization in MQWs.[18] The stress-relaxed InGaN film is also proven to have more pronounced carrier localization than the strained InGaN film.[34,47] Therefore, both of the improved crystal quality and stress relaxation of the underlying GaN template lead to the stronger carrier localization of MQWs on SCPSS. In light of the above TDPL findings, the reduced TDs and increased localization effects enable more carriers trapped by localized states and fewer by dislocations, leading to the suppressed nonradiative recombination in the MQW sample on SCPSS.

DOI: 10.1021/acsami.6b07044
ACS Appl. Mater. Interfaces XXXX, XXX, XXX−XXX

Figure 7c shows the excitation power-dependent variations of the PL peak energy and line width at RT. As the excitation power increases from 2 to 46 mW, the peak energy shows a buleshift of 3.3 and 10.6 meV respectively, accompanied by a gradual decrease in fwhm (in the inset). It is known that the carrier screening of quantum confined Stark effect (QCSE) can induce a blueshift of the peak energy and decrease of line width with increasing excitation power.[48] The much smaller blueshift suggests weaker QCSE in MQWs on SCPSS, arising from the reduced piezoelectric field weakened by the stress relaxation.[49] Therefore, the reduced QCSE of MQWs on SCPSS is demonstrated, conforming to the Raman results. Its influence on the radiative recombination rate will be discussed next.

To further investigate the recombination dynamics in MQWs, we conducted time-resolved PL (TRPL) measurements under the same pump density at 10 K and RT. The radiative recombination can be conspicuously studied at 10 K, because the nonradiative recombination is almost frozen at low temperature.[50] The PL decay traces at 10 K for emission peaks are illustrated in Figure 8a. The PL decay curves can be well-fitted by biexponential decaying function[50,51]

$$I(t) = A_1\exp(-t/\tau_1) + A_2\exp(-t/\tau_2) \quad (2)$$

where the fast decay time τ_1 represents radiative recombination of free excitons and the relaxation of excitons from free or extended states to localized states, and the slow decay time τ_2 describes transport among localized states and the radiative lifetime of localized excitons. Note that at 10 K, MQWs on SCPSS exhibit shorter lifetimes of τ_1 = 1.41 ns and τ_2 = 8.19 ns for both fast and slow decays, whereas MQWs on CSS has lifetimes of τ_1 = 2.20 ns and τ_2 = 14.08 ns. The shorter lifetimes of MQWs on SCPSS indicate faster rates and hence higher efficiency of radiative recombination. We believe that the electron−hole wave function overlap is enlarged because of the reduced less piezoelectric field and QCSE on SCPSS, increasing the radiative recombination rates and IQE.[49,52] Moreover, the radiative (τ_r) and nonradiative (τ_{nr}) lifetimes at RT can be derived from[52] $1/\tau_{PL} = 1/\tau_r + 1/\tau_{nr}$ and $\eta_{int} = 1/(1 + \tau_r/\tau_{nr})$, where IQE ($\eta_{int}$) at RT has been calculated in Figure 7a, and the representative decay lifetime (τ_{PL}) can be obtained from Figure 8b. The weight ratio $A_1/(A_1 + A_2)$ exceeds 87% for both samples. It means the fast decay τ_1 dominates the overall PL decay and can be taken as τ_{PL} for MQWs on SCPSS (2.01 ns) and on CSS (2.15 ns) at RT. As a consequence, the MQW sample on SCPSS has a shorter radiative lifetime τ_r (5.31 ns) and a longer nonradiative lifetime τ_{nr} (3.24 ns), compared with τ_r(8.61 ns) and τ_{nr} (2.87 ns) of MQWs on CSS, proving enhanced radiative recombination and suppressed nonradiative recombination. Thus, the reduced nonradiative recombination centers, the enhanced carrier localization and the suppressed QCSE are jointly responsible for the significantly improved performance featured by the SCPSS-based MQW structure.

CONCLUSIONS

In summary, we have developed an innovative ELOG technique based on SCPSS without regrowth and further optimization, which can greatly decrease the dislocation density. To obtain the fully coalescent GaN, the lateral growth rates in different ELOG stages were carefully modulated according to the shape of serpentine channel mask. In addition, periodical spatial variations on the crystal quality and stress state are elaborately identified in GaN epilayers on the mask. The contiguous area of low defect density GaN is expanded to both the wing and window regions on SCPSS. Moreover, IQE of the MQW sample on SCPSS is proved to be 52% higher than that on CSS. Here, the reduced defect density and the relaxed stress jointly contribute to the enhanced performance of InGaN MQWs on SCPSS. In essence, the device performance should be more outstanding if all wing and window regions are connected together while periodic coalescence region is etched away. The sufficient dislocation blocking from the serpentine channel patterned mask opens up a production route for growing polar/semipolar/nonpolar-plane GaN-based devices with high quality on substrate with severe mismatch like Si substrate, etc.

ASSOCIATED CONTENT

Supporting Information

The Supporting Information is available free of charge on the ACS Publications website at DOI: 10.1021/acsami.6b07044.

Fabrication process of serpentine channel patterned sapphire substrate as well as the calculations of the indium composition of MQWs determined by simulations of HRXRD $\omega-2\theta$ scans of (0002)-plane; cross-sectional TEM bright-field images of GaN in different regions on SCPSS with different two-beam conditions (PDF)

AUTHOR INFORMATION

Corresponding Authors

*E-mail: chenwh@pku.edu.cn.
*E-mail: huxd@pku.edu.cn.

Notes

The authors declare no competing financial interest.

ACKNOWLEDGMENTS

This work was supported by the National Natural Science Foundation of China (Grants 61334005, 51272008, and 11505015), the Key National Research and Development Program (Grant No. 2016YFB0401801), and the National Basic Research Program of China (Grant No. 2014CB846001). Y.H.X. acknowledges the support from Alexander von Humboldt Foundation Research Award. The authors thank all the staff involved during the measurements at the beamline 1W1A at BSRF.

REFERENCES

(1) Gibart, P. Metal Organic Vapour Phase Epitaxy of GaN and Lateral Overgrowth. *Rep. Prog. Phys.* **2004**, *67*, 667−715.
(2) Nakamura, S. The Roles of Structural Imperfections in InGaN-Based Blue Light-Emitting Diodes and Laser Diodes. *Science* **1998**, *281*, 956−961.
(3) Schubert, M. F.; Chhajed, S.; Kim, J. K.; Schubert, E. F.; Koleske, D. D.; Crawford, M. H.; Lee, S. R.; Fischer, A. J.; Thaler, G.; Banas, M. A. Effect of Dislocation Density on Efficiency Droop in GaInN/GaN Light-Emitting Diodes. *Appl. Phys. Lett.* **2007**, *91*, 231114.
(4) Ťapajna, M.; Kaun, S. W.; Wong, M. H.; Gao, F.; Palacios, T.; Mishra, U. K.; Speck, J. S.; Kuball, M. Influence of Threading Dislocation Density on Early Degradation in AlGaN/GaN High Electron Mobility Transistors. *Appl. Phys. Lett.* **2011**, *99*, 223501.
(5) Li, D.; Sun, X.; Song, H.; Li, Z.; Chen, Y.; Miao, G.; Jiang, H. Influence of Threading Dislocations on GaN-Based Metal-Semiconductor-Metal Ultraviolet Photodetectors. *Appl. Phys. Lett.* **2011**, *98*, 011108.
(6) Khan, A.; Balakrishnan, K.; Katona, T. Ultraviolet Light-Emitting Diodes Based on Group Three Nitrides. *Nat. Photonics* **2008**, *2*, 77−84.

(7) Hiramatsu, K.; Nishiyama, K.; Onishi, M.; Mizutani, H.; Narukawa, M.; Motogaito, A.; Miyake, H.; Iyechika, Y.; Maeda, T. Fabrication and Characterization of Low Defect Density Gan Using Facet-Controlled Epitaxial Lateral Overgrowth (FACELO). *J. Cryst. Growth* **2000**, *221*, 316−326.
(8) Zheleva, T. S.; Smith, S. A.; Thomson, D. B.; Linthicum, K. J.; Rajagopal, P.; Davis, R. F. Pendeo-Epitaxy: A New Approach for Lateral Growth of Gallium Nitride Films. *J. Electron. Mater.* **1999**, *28*, L5−L8.
(9) Polyakov, A. Y.; Govorkov, A. V.; Smirnov, N. B.; Markov, A. V.; Lee, I.-H.; Ju, J.-W.; Karpov, S. Y.; Shmidt, N. M.; Pearton, S. J. Properties of Undoped GaN/InGaN Multi-Quantum-Wells and GaN/InGaN P-N Junctions Prepared by Epitaxial Lateral Overgrowth. *J. Appl. Phys.* **2009**, *105*, 123708.
(10) Song, J. S.; Rho, H.; Jeong, M. S.; Ju, J. W.; Lee, I. H. Spatially Resolved Photoluminescence and Raman Mapping of Epitaxial GaN Laterally Overgrown on Sapphire. *Phys. Rev. B: Condens. Matter Mater. Phys.* **2010**, *81*, 200304.
(11) Fong, W. K.; Leung, K. K.; Surya, C. Growth and Characterization of GaN/InGaN Multiple Quantum Wells on Nanoscale Epitaxial Lateral Overgrown Layers. *Cryst. Growth Des.* **2011**, *11*, 2091−2097.
(12) Zhang, L.; Li, X.; Shao, Y.; Yu, J.; Wu, Y.; Hao, X.; Yin, Z.; Dai, Y.; Tian, Y.; Huo, Q.; Shen, Y.; Hua, Z.; Zhang, B. Improving the Quality of GaN Crystals by Using Graphene or Hexagonal Boron Nitride Nanosheets Substrate. *ACS Appl. Mater. Interfaces* **2015**, *7*, 4504−4510.
(13) Seo, T. H.; Park, A. H.; Park, S.; Kim, Y. H.; Lee, G. H.; Kim, M. J.; Jeong, M. S.; Lee, Y. H.; Hahn, Y. B.; Suh, E. K. Direct Growth of GaN Layer on Carbon Nanotube-Graphene Hybrid Structure and Its Application for Light Emitting Diodes. *Sci. Rep.* **2015**, *5*, 7747.
(14) Park, A. H.; Seo, T. H.; Chandramohan, S.; Lee, G. H.; Min, K. H.; Lee, S.; Kim, M. J.; Hwang, Y. G.; Suh, E. K. Efficient Stress-Relaxation in InGaN/GaN Light-Emitting Diodes Using Carbon Nanotubes. *Nanoscale* **2015**, *7*, 15099−15105.
(15) Vennéguès, P. Defect Reduction Methods for III-Nitride Heteroepitaxial Films Grown Along Nonpolar and Semipolar Orientations. *Semicond. Sci. Technol.* **2012**, *27*, 024004.
(16) Haskell, B. A.; Wu, F.; Craven, M. D.; Matsuda, S.; Fini, P. T.; Fujii, T.; Fujito, K.; DenBaars, S. P.; Speck, J. S.; Nakamura, S. Defect Reduction in $(11\bar{2}0)$ a-Plane Gallium Nitride Via Lateral Epitaxial Overgrowth by Hydride Vapor-Phase Epitaxy. *Appl. Phys. Lett.* **2003**, *83*, 644−646.
(17) Freitas, J. A.; Culbertson, J. C.; Mahadik, N. A.; Sochacki, T.; Bockowski, M.; Iwinska, M. Growth of High Crystalline Quality HVPE-GaN Crystals with Controlled Electrical Properties. *Cryst. Growth Des.* **2015**, *15*, 4837−4842.
(18) Jeong, H.; Jeong, H. J.; Oh, H. M.; Hong, C. H.; Suh, E. K.; Lerondel, G.; Jeong, M. S. Carrier Localization in In-Rich InGaN/GaN Multiple Quantum Wells for Green Light-Emitting Diodes. *Sci. Rep.* **2015**, *5*, 9373.
(19) Akita, K.; Kyono, T.; Yoshizumi, Y.; Kitabayashi, H.; Katayama, K. Improvements of External Quantum Efficiency of InGaN-Based Blue Light-Emitting Diodes at High Current Density Using GaN Substrates. *J. Appl. Phys.* **2007**, *101*, 033104.
(20) Sun, Q.; Yerino, C. D.; Leung, B.; Han, J.; Coltrin, M. E. Understanding and Controlling Heteroepitaxy with the Kinetic Wulff Plot: A Case Study with GaN. *J. Appl. Phys.* **2011**, *110*, 053517.
(21) Tripathy, S.; Chua, S. J.; Hao, M. S.; Sia, E. K.; Ramam, A.; Zhang, J.; Sun, W. H.; Wang, L. S. Micro-Raman Scattering in Laterally Epitaxial Overgrown GaN. *J. Appl. Phys.* **2002**, *91*, 5840−5852.
(22) Paskova, T.; Arnaudov, B.; Paskov, P. P.; Goldys, E. M.; Hautakangas, S.; Saarinen, K.; Södervall, U.; Monemar, B. Donor-Acceptor Pair Emission Enhancement in Mass-Transport-Grown GaN. *J. Appl. Phys.* **2005**, *98*, 033508.
(23) Wagner, V.; Parillaud, O.; Bühlmann, H. J.; Ilegems, M.; Gradecak, S.; Stadelmann, P.; Riemann, T.; Christen, J. Influence of the Carrier Gas Composition on Morphology, Dislocations, and Microscopic Luminescence Properties of Selectively Grown GaN by Hydride Vapor Phase Epitaxy. *J. Appl. Phys.* **2002**, *92*, 1307.
(24) Kaschner, A.; Hoffmann, A.; Thomsen, C.; Bertram, F.; Riemann, T.; Christen, J.; Hiramatsu, K.; Sone, H.; Sawaki, N. Micro-Raman and Cathodoluminescence Studies of Epitaxial Laterally Overgrown GaN with Tungsten Masks: A Method to Map the Free-Carrier Concentration of Thick GaN Samples. *Appl. Phys. Lett.* **2000**, *76*, 3418−3420.
(25) Chaldyshev, V. V.; Pollak, F. H.; Pophristic, M.; Guo, S. P.; Ferguson, I. Micro-Raman Investigation of Thin Lateral Epitaxial Overgrown GaN/Sapphire(0001) Films. *J. Appl. Phys.* **2002**, *92*, 6601.
(26) Teisseyre, H.; Kamińska, A.; Franssen, G.; Dussaigne, A.; Grandjean, N.; Grzegory, I.; Łucznik, B.; Suski, T. Different Pressure Behavior of GaN/AlGaN Quantum Structures Grown Along Polar and Nonpolar Crystallographic Directions. *J. Appl. Phys.* **2009**, *105*, 063104.
(27) Weyher, J. L.; Lazar, S.; Macht, L.; Liliental-Weber, Z.; Molnar, R. J.; Müller, S.; Sivel, V. G. M.; Nowak, G.; Grzegory, I. Orthodox Etching of HVPE-Grown GaN. *J. Cryst. Growth* **2007**, *305*, 384−392.
(28) Zhang, W.; Liu, P.; Jackson, B.; Sun, T.; Huang, S.-J.; Hsu, H.-C.; Su, Y.-K.; Chang, S.-J.; Li, L.; Li, D.; Wang, L.; Hu, X.; Xie, Y. H. Dislocation Reduction through Nucleation and Growth Selectivity of Metal-Organic Chemical Vapor Deposition GaN. *J. Appl. Phys.* **2013**, *113*, 144908.
(29) Li, L.; Liu, J. P. C.; Liu, L.; Li, D.; Wang, L.; Wan, C.; Chen, W.; Yang, Z.; Xie, Y.; Hu, X.; Zhang, G. Defect Reduction Via Selective Lateral Epitaxy of GaN on an Innovative Masked Structure with Serpentine Channels. *Appl. Phys. Express* **2012**, *5*, 051001.
(30) Zheleva, T. S.; Nam, O.-H.; Ashmawi, W. M.; Griffin, J. D.; Davis, R. F. Lateral Epitaxy and Dislocation Density Reduction in Selectively Grown GaN Structures. *J. Cryst. Growth* **2001**, *222*, 706−718.
(31) Mei, J.; Srinivasan, S.; Liu, R.; Ponce, F. A.; Narukawa, Y.; Mukai, T. Prismatic Stacking Faults in Epitaxially Laterally Overgrown Gan. *Appl. Phys. Lett.* **2006**, *88*, 141912.
(32) Benyoucef, M.; Kuball, M.; Beaumont, B.; Gibart, P. Raman Mapping, Photoluminescence Investigations, and Finite Element Analysis of Epitaxial Lateral Overgrown GaN on Silicon Substrates. *Appl. Phys. Lett.* **2002**, *80*, 2275−2277.
(33) Ryu, J. H.; Katharria, Y. S.; Kim, H. Y.; Kim, H. K.; Ko, K. B.; Han, N.; Kang, J. H.; Park, Y. J.; Suh, E. K.; Hong, C. H. Stress-Relaxed Growth of n-GaN Epilayers. *Appl. Phys. Lett.* **2012**, *100*, 181904.
(34) Soh, C. B.; Chow, S. Y.; Tan, L. Y.; Hartono, H.; Liu, W.; Chua, S. J. Enhanced Luminescence Efficiency Due to Carrier Localization in InGaN/GaN Heterostructures Grown on Nanoporous GaN Templates. *Appl. Phys. Lett.* **2008**, *93*, 173107.
(35) Park, Y. J.; Kim, H. K.; Katharria, Y. S.; Han, N.; Han, M.; Ryu, B. D.; Ko, K. B.; Yang, J. H.; Kim, Y. T.; Suh, E.-K.; Song, J.-H.; Hong, C.-H. Investigations of the Air Gap Embedded Green InGaN/GaN Light-Emitting Diodes. *Appl. Phys. Express* **2013**, *6*, 072104.
(36) Lee, K. J.; Kim, S. J.; Kim, J. J.; Hwang, K.; Kim, S. T.; Park, S. J. Enhanced Performance of InGaN/GaN Multiple-Quantum-Well Light-Emitting Diodes Grown on Nanoporous GaN Layers. *Opt. Express* **2014**, *22*, A1164−A1173.
(37) Nagarajan, S.; Svensk, O.; Ali, M.; Naresh-Kumar, G.; Trager-Cowan, C.; Suihkonen, S.; Sopanen, M.; Lipsanen, H. Stress Distribution of GaN Layer Grown on Micro-Pillar Patterned GaN Templates. *Appl. Phys. Lett.* **2013**, *103*, 012102.
(38) Kontos, A. G.; Raptis, Y. S.; Pelekanos, N. T.; Georgakilas, A.; Bellet-Amalric, E.; Jalabert, D. Micro-Raman Characterization of $In_xGa_{1-x}N/GaN/Al_2O_3$ heterostructures. *Phys. Rev. B: Condens. Matter Mater. Phys.* **2005**, *72*, 155336.
(39) Han, S.-H.; Cho, C.-Y.; Lee, S.-J.; Park, T.-Y.; Kim, T.-H.; Park, S. H.; Won Kang, S.; Won Kim, J.; Kim, Y. C.; Park, S.-J. Effect of Mg Doping in the Barrier of InGaN/GaN Multiple Quantum Well on Optical Power of Light-Emitting Diodes. *Appl. Phys. Lett.* **2010**, *96*, 051113.

DOI: 10.1021/acsami.6b07044
ACS Appl. Mater. Interfaces XXXX, XXX, XXX−XXX

(40) Cho, C.-Y.; Kwon, M.-K.; Park, I.-K.; Hong, S.-H.; Kim, J.-J.; Park, S.-E.; Kim, S.-T.; Park, S.-J. High-Efficiency Light-Emitting Diode with Air Voids Embedded in Lateral Epitaxially Overgrown GaN Using a Metal Mask. *Opt. Express* **2011**, *19*, A943−A948.
(41) Abell, J.; Moustakas, T. D. The Role of Dislocations as Nonradiative Recombination Centers in InGaN Quantum Wells. *Appl. Phys. Lett.* **2008**, *92*, 091901.
(42) Naranjo, F. B.; Sánchez-García, M. A.; Calle, F.; Calleja, E.; Jenichen, B.; Ploog, K. H. Strong Localization in InGaN Layers with High In Content Grown by Molecular-Beam Epitaxy. *Appl. Phys. Lett.* **2002**, *80*, 231−233.
(43) Gačević, Z.; Das, A.; Teubert, J.; Kotsar, Y.; Kandaswamy, P. K.; Kehagias, T.; Koukoula, T.; Komninou, P.; Monroy, E. Internal Quantum Efficiency of III-Nitride Quantum Dot Superlattices Grown by Plasma-Assisted Molecular-Beam Epitaxy. *J. Appl. Phys.* **2011**, *109*, 103501.
(44) Noh, Y.-K.; Seo, J.-H.; Choi, H.-S.; Kim, M.-D.; Oh, J.-E. Thickness Dependence of Temperature-Induced Emission Mechanism in InGaN/AlGaN Short-Period Superlattices. *J. Appl. Phys.* **2012**, *112*, 043102.
(45) Ko, S.-M.; Kwack, H.-S.; Park, C.; Yoo, Y.-S.; Kwon, S.-Y.; Jin Kim, H.; Yoon, E.; Si Dang, L.; Cho, Y.-H. Strong Carrier Localization and Diminished Quantum-Confined Stark Effect in Ultra-Thin High-Indium-Content InGaN Quantum Wells with Violet Light Emission. *Appl. Phys. Lett.* **2013**, *103*, 222104.
(46) Franssen, G.; Suski, T.; Kryśko, M.; Khachapuridze, A.; Kudrawiec, R.; Misiewicz, J.; Kamińska, A.; Feltin, E.; Grandjean, N. Built-in Electric Field and Large Stokes Shift in near-Lattice-Matched GaN/AlInN Quantum Wells. *Appl. Phys. Lett.* **2008**, *92*, 201901.
(47) Tsai, W. C.; Hsu, C. H.; Fu, S. F.; Lee, F. W.; Chen, C. Y.; Chou, W. C.; Chen, W. K.; Chang, W. H. Optical Properties Associated with Strain Relaxations in Thick InGaN Epitaxial Films. *Opt. Express* **2014**, *22*, A416−A424.
(48) Lai, Y.-L.; Liu, C.-P.; Lin, Y.-H.; Hsueh, T.-H.; Lin, R.-M.; Lyu, D.-Y.; Peng, Z.-X.; Lin, T.-Y. Origins of Efficient Green Light Emission in Phase-Separated InGaN Quantum Wells. *Nanotechnology* **2006**, *17*, 3734−3739.
(49) Kawakami, Y.; Kaneta, A.; Su, L.; Zhu, Y.; Okamoto, K.; Funato, M.; Kikuchi, A.; Kishino, K. Optical Properties of InGaN/GaN Nanopillars Fabricated by Postgrowth Chemically Assisted Ion Beam Etching. *J. Appl. Phys.* **2010**, *107*, 023522.
(50) Ko, T. S.; Lu, T. C.; Wang, T. C.; Lo, M. H.; Chen, J. R.; Gao, R. C.; Kuo, H. C.; Wang, S. C.; Shen, J. L. Optical Characteristics of a-Plane InGaN/GaN Multiple Quantum Wells with Different Well Widths. *Appl. Phys. Lett.* **2007**, *90*, 181122.
(51) Li, Z.; Kang, J.; Wei Wang, B.; Li, H.; Hsiang Weng, Y.; Lee, Y.-C.; Liu, Z.; Yi, X.; Chuan Feng, Z.; Wang, G. Two Distinct Carrier Localization in Green Light-Emitting Diodes with InGaN/GaN Multiple Quantum Wells. *J. Appl. Phys.* **2014**, *115*, 083112.
(52) Deshpande, S.; Frost, T.; Yan, L.; Jahangir, S.; Hazari, A.; Liu, X.; Mirecki-Millunchick, J.; Mi, Z.; Bhattacharya, P. Formation and Nature of InGaN Quantum Dots in GaN Nanowires. *Nano Lett.* **2015**, *15*, 1647−1653.

DOI: 10.1021/acsami.6b07044
ACS Appl. Mater. Interfaces XXXX, XXX, XXX−XXX